Biosensors and Bioelectronics 132 (2019) 8–16

Contents lists available at ScienceDirect

Biosensors and Bioelectronics

journal homepage: www.elsevier.com/locate/bios

Covalent organic framework-based electrochemical aptasensors for the ultrasensitive detection of antibiotics

Minghua Wang, Mengyao Hu, Jiameng Liu, Chuanpan Guo, Donglai Peng, Qiaojuan Jia, Linghao He, Zhihong Zhang*, Miao Du*

Henan Provincial Key Laboratory of Surface and Interface Science, Zhengzhou University of Light Industry, No. 136, Science Avenue, Zhengzhou 450001, PR China

ARTICLE INFO

Keywords:
Covalent organic framework
Label-free aptasensor
Detection of enrofloxacin
Detection of ampicillin
Electrochemical impedance spectroscopy

ABSTRACT

We designed and synthesized a novel covalent organic framework (COF) by condensation polymerization of 1,3,6,8-tetrakis(4-formylphenyl)pyrene and melamine through imine bonds (represented by Py-M-COF). The basic characterizations revealed that the Py-M-COF not only exhibited an extended π-conjugation framework, a large specific surface area (495.5 $m^2 g^{-1}$), big pore cavities, and nanosheet-like structure but also possessed rich functional groups, such as C=C, C=N, C=O, and NH_2. These features endowed the Py-M-COF with high charge carrier mobility, further improving the strong immobilization of DNA aptamer strands via π-π stacking interaction and electrostatic interaction. As such, the Py-M-COF-based electrochemical aptasensors are ultrasensitive in detecting different antibiotics, including enrofloxacin (ENR) and ampicillin (AMP), yielding extremely low detection limits of 6.07 and 0.04 fg mL^{-1} (S/N = 3) toward ENR and AMP, respectively, along with other excellent sensing performances. This biosensing platform based on Py-M-COF has potential applications for the sensitive detection of antibiotics or other analytes by replacing the corresponding aptamers.

1. Introduction

Recently, the increase in antibiotic-resistant microorganisms is a challenge for consumer health protection and veterinary medicine. According to the Centers for Disease Control and Prevention, about 23,000 deaths that occur annually in the United States are related to infections caused by antibiotic-resistant bacteria (Syska, 2013). Inappropriate and prophylactic use of antibiotics (especially in the field of animal care) is common. It may bring negative influence on human health and the environment, such as toxicity to organs and disruption of the ecological balance. Among many antibiotics, enrofloxacin (ENR) is a fluoroquinolone antibiotic that has been extensively used to prevent and treat bacterial diseases in livestock and aquaculture (Tang et al., 2017). Ampicillin (AMP) is a broad-spectrum β-lactam group antibiotic that is widely used in medicine because of its ability to destroy Gram-positive and Gram-negative bacteria with cell wall breaking mechanism (Körbahti and Taşyürek, 2015). Consequently, the development of portable, high-throughput, and inexpensive detection systems is particularly attractive and urgently desired, especially in underdeveloped areas.

Aptamers are artificial single-stranded DNA or RNA molecules with specific 3D structures selected in vitro through SELEX (Li et al., 2018). Aptamers have attracted tremendous interest as recognition probes in bioassays because of their high selectivity, simple synthesis, easy modification, and good stability (Huang et al., 2017). Numerous analytical methods, such as fluorescence (Luo et al., 2017), electrochemistry (Yang et al., 2017b), surface plasma resonance (Pan et al., 2017), and chemiluminescence (Yu et al., 2014), have been reported for ENR and AMP detection. However, these instrument-based methods require expensive and elaborate instrumentation, so they are unsuitable for on-site applications. DNA-functionalized gold nanoparticles were used to determine AMP, providing a limit of detection (LOD) of 0.38 pM within its concentration from 1 pM to 5 nM (Wang et al., 2017). A fluorescent sensing system based on graphene oxide was developed, and the LOD for ENR determination was 3.7 nM within the linear range of 5–250 nM (Dolati et al., 2018). These reported bioassays showed relatively simple operation compared with the conventional labeling methods, but they involved complicated assembly processes and low sensitivity. The combination of aptamers with electrochemical detection methods leads to sensitive, fast, simple, and cost-effective biosensors (Du et al., 2007). Electrochemical aptasensors can benefit from two main approaches, namely, covalently labeled aptamers (with enzymes, metal nanoparticles, and redox compound) and label-free techniques, for detecting the target. In terms of electrochemical sensors,

* Corresponding authors.
E-mail addresses: 2006025@zzuli.edu.cn (Z. Zhang), dumiao@zzuli.edu.cn (M. Du).

https://doi.org/10.1016/j.bios.2019.02.040
Received 13 December 2018; Received in revised form 8 February 2019; Accepted 13 February 2019
Available online 21 February 2019
0956-5663/ © 2019 Elsevier B.V. All rights reserved.

impedance techniques are useful in monitoring biorecognition events and their changes in electrical properties at the surfaces of modified electrodes. Electrochemical impedance spectroscopy (EIS) is a simple, sensitive, and rapid approach (Zhang et al., 2018) that has been widely used for detecting signals generated by binding the analyte to its targeted aptamer on the transducer surface. Nanomaterials and nanocomposites have been used to increase the electroactive area, increase the loading with aptamer, and provide 3D support, thereby facilitating aptamer immobilization and minimizing steric hindrances (Soler, 2018). Aptamer immobilization on the transducer surface is a determining step for the performance of the obtained aptasensor. The most common approaches ensure adequate stability and surface coverage by aptamers and maintain the same binding affinity as displayed in a solution. Although various nanostructured materials and signal amplification strategies (e.g., gold nanoparticles (Liu et al., 2015b), bimetallic nanoparticles (Xu et al., 2015), functionalized graphene (Qin et al., 2016), carbon nanotubes (Chen et al., 2015), graphene quantum dots (Huang et al., 2017), and metal-organic frameworks (Yang et al., 2017a; Zhang et al., 2017)) have been employed to fabricate electrochemical aptasensors for detecting antibiotics, the search for new types of materials with predictable structures, large specific surface area, and excellent machinability to effectively immobilize aptamers and improve the detecting sensitivity remains challenging.

As a new type of crystalline porous material, covalent organic frameworks (COFs) are solely constructed with organic building blocks containing light elements (e.g., C, N, O, H, and B) and linked by strong covalent bonds (Chen et al., 2018). Given their large specific surface areas, ordered pore structure, tunable functionality, low density, and mechanical robustness (Ding et al., 2016), various sensing platforms, such as chemical sensor (Gao et al., 2018), humidity sensing (Singh et al., 2017), fluorescent sensor (Li et al., 2016), and colorimetric pH sensor (Chen et al., 2018), have been used for detecting nitroaromatic explosives, small organic molecules, heavy metal ions, and volatile organic compounds (Das and Mandal, 2018; Ding et al., 2016; Xiang and Cao, 2012; Zhang et al., 2012). On the basis of the construction principle of COFs, ideal biosensing platforms can be achieved by the rational design of controllable structures. For instance, TpTta comprising 1,3,5-triformylphloroglucinol (Tp) and 4,40,400-(1,3,5-triazine-2,4,6-triyl) trianiline (Tta) (Li et al., 2017), 2D ionic covalent organic nanosheets (Sun et al., 2017), and TPA-COF (Chen et al., 2017) were prepared as bioplatforms to selectively detect double-stranded DNA through π-π stacking and hydrogen-bonding interactions. However, most COFs have poor electrochemical activity, and their applications as electrochemical biosensor platforms are limited. In particular, studies on COF-based electrochemical aptasensors are still not fully explored. COFs with rich π-conjugation frameworks and functional groups may be considered new candidates for aptamer attachment via π-π stacking interaction (Zhai et al., 2019). Moreover, their 2D/3D architecture with permanent porosity offers an excellent scaffold for charge migration and molecule diffusion over the network and improves sensitivity through signal amplification (Medina et al., 2017). Considering the inherent features of COFs, it is extremely interesting to develop electrochemical aptasensors based on COF materials for sensitive and selective detection of targets.

To fabricate ultrasensitive biosensing platforms for detecting antibiotics, we designed and synthesized a novel COF via condensation of 1,3,6,8-tetrakis(4-formylphenyl)pyrene (TFPPy) and melamine (M) through imine bonds (-C=N-) (represented by Py-M-COF) for the first time (Scheme 1**a**). The Py-M-COF was further used as a scaffold for aptamer strands immobilization to sensitively detect antibiotics, specifically ENR and AMP (Scheme 1**b**). For comparison, the graphitic carbon nitride (g-C_3N_4) and amino-functionalized graphene oxide (GO-NH_2) nanosheets were modified with TFPPy (denoted as Py-g-C_3N_4 and Py-GO, respectively) and used as scaffolds for aptasensors for detecting ENR antibiotic. Electrochemical results revealed that the Py-M-COF-based aptasensor exhibited the most sensitive detection efficiency for antibiotic among three kinds of aptasensors.

2. Experimental section

The parts of chemical and materials, preparation of all solutions, pretreatment of the bare gold electrode, and basic characterizations were supplied in S1 (See the Supplementary material).

2.1. Synthesis of Py-M-COF, Py-g-C_3N_4 and Py-GO

Typically, 6 mg 1,3,6,8-Tetrakis(4-formylphenyl)pyrene (TFPPy) was dissolved in 6 mL of dimethyl sulfoxide. Subsequently, 10 mg melamine was put in the above mixture and oil bath (150 °C) for 48 h. The product was washed with tetrahydrofuran and ethanol repeatedly for several times and then dried at 60 °C in oven to yield the Py-M-COF powder.

The g-C_3N_4 was synthesized by polymerization of melamine reported in the literature (Zhang et al., 2013). GO and GO-NH_2 was prepared according to our previously reported (Wang et al., 2015b). The Py-g-C_3N_4 and Py-GO hybrids were synthesized in the similar manner as that of Py-M-COF by adding 10 mg g-C_3N_4 and 10 mg GO-NH_2 instead of melamine, separately.

2.2. Fabrication of the Py-M-COF-based aptasensors

1 mg Py-M-COF was added to 1 mL of Milli-Q water and sonicated thoroughly until a homogeneous suspension was obtained. In terms of Py-M-COF-based aptasensor fabrication, 10.0 μL of Py-M-COF suspension (1.0 mg mL^{-1}) was dropped onto the pre-treated bare Au electrode (AE) (represented by Py-M-COF/AE). Subsequently, the modified AE was immersed in the aptamer solutions of ENR and AMP for 2 h at 4 °C, separately (represented by Apt_{ENR}/Py-M-COF/AE and Apt_{AMP}/Py-M-COF/AE, respectively). The modified AE was sufficiently rinsed with PBS and dried over a gentle stream of N_2, through which the developed Apt_{ENR}/Py-M-COF/AE and Apt_{AMP}/Py-M-COF/AE aptasensors were accomplished. Following the same steps, Apt_{ENR}/Py-g-C_3N_4/AE and Apt_{ENR}/Py-GO/AE aptasensors were also obtained. All developed aptasensors were stored in 4 °C refrigerator for further use.

2.3. Electrochemical measurements

Cyclic voltammetry (CV) and electrochemical impedance spectroscopy (EIS) were conducted on the CHI 660E electrochemical station. A traditional three-electrode system including a bare or modified AE as the working electrode, an Ag/AgCl (3 M KCl) as the reference electrode, and a platinum wire as the auxiliary electrode was used in the electrochemical measurements. CV curves was performed from −0.2–0.8 V at the scan rate of 50 mV s^{-1} in PBS solution (pH 7.4, 0.01 M) containing 5 mM $[Fe(CN)_6]^{3-/4-}$. EIS was carried out within the frequency range of 0.01 Hz-100 kHz with amplitude of 5 mV under open circuit potential of 0.22 V. The EIS spectra were analyzed using ZView2 software, which was obtained from Scribner Associates Incorporated (Fig. S1). The software utilizes nonlinear least-squares fitting to determine the parameters of the elements in the equivalent circuit (Fig. S1, the inset), which is consisted of solution resistance (R_s), charge-transfer resistance (R_{ct}), constant-phase element (*CPE*), and Warburg impedance (*W*).

The as-fabricated aptasensors were immersed in ENR or AMP solutions with different concentrations during electrochemical measurements to determine the sensitivity and detection limit of the aptasensor toward the analyte (denoted as ENR/Apt_{ENR}/Py-M-COF/AE and AMP/Apt_{AMP}/Py-M-COF/AE, respectively). The selectivity of the aptasensor was determined by incubation with tetracycline, kanamycin (Kana), tobramycin (TOB), Na^+, K^+, streptomycin, and oxytetracycline (OTC) at room temperature. The reproducibility was evaluated by preparing five aptasensors independently. For stability assessment, the aptasensor

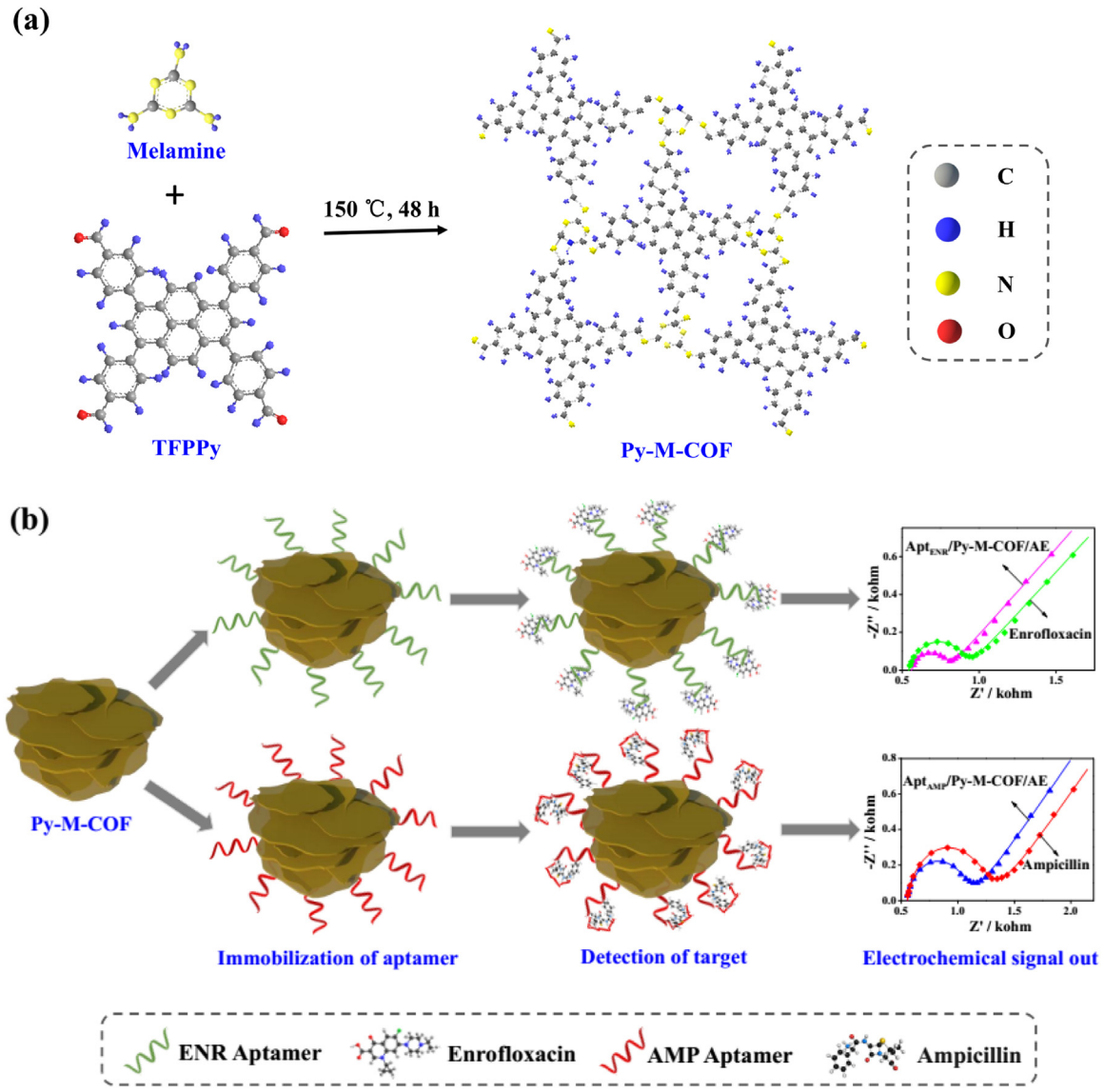

Scheme 1. (a) Scheme of the synthesis of Py-M-COF. (b) Scheme of electrochemical detection of ENR and AMP using the Py-M-COF-based aptasensors.

was stored at 4 °C for 15 days and measured by EIS every day. Human serum sample was used to verify the applicability of the developed aptasensors.

3. Results and discussion

3.1. Design mechanism of the Py-M-COF-based aptasensors

The proposed strategy for detecting antibiotics is depicted in Scheme 1**b**. The Py-M-COF scaffolds were anchored with aptamers through π-π stacking and electrostatic interactions (Gao et al., 2018). Label-free aptamer strands, including ENR-targeted aptamer (Apt_{ENR}, 5′-CCC ATC AGG GGG CTA GGC TAA CAC GGT TCG GCT CTC TGA GCC CGG GTT ATT TCA GGG GGA-3′) (Liu et al., 2017a, 2017b) and AMP-targeted aptamer (Apt_{AMP}, 5′-TTA GTT GGG GTT CAG TTG G-3′) (Song et al., 2012), were used to recognize ENR and AMP molecules, respectively. When introducing ENR, the folding of Apt_{ENR} upon the existing target is preferred to form the aptamer-ENR complex (Liu et al., 2017b). In terms of AMP aptasensor, the binding of target AMP induces a change in the aptamer conformation and flexibility (Yu et al., 2018). Each process can alter charge transfer, leading to variations in the electrochemical signals. Thus, the detection steps of target molecules can be determined by electrochemical techniques.

3.2. Crystal and chemical structure of as-synthesized Py-M-COF

The crystal and chemical structure of Py-M-COF were characterized by powder X-ray diffraction measurements (PXRD), Fourier transform infrared spectroscopy (FT-IR), ^{13}C nuclear magnetic resonance (NMR), and X-ray photoelectron spectroscopy (XPS). The XRD of Py-M-COF was simulated, whereas the structure model was generated with Materials Studio. The atom coordinates were optimized by DFTB+ based on the Density Functional Tight Binding (DFTB) method. The Py-M-COF was presumed to be crystallized in the orthorhombic system, space group *P*222 with $a = 43.21803$, $b = 55.35925$, $c = 43.40755$ Å, $R_{wp} = 6.95\%$, $R_p = 5.14\%$. As shown in Fig. 1**a**, the simulated and synthesized XRD patterns show a good agreement. According to the Debye-Scherrer formula (Guillerm et al., 2010), the average particle size of the Py-M-COF was estimated to be around 52.94 nm. Fig. 1**b** shows the FT-IR spectra of TFPPy, melamine, and Py-M-COF. The characteristic peak at 1698 cm^{-1} was ascribed to the C=O stretching band of TFPPy (curve *i*), whereas the peaks at 3469, 3419 and 3336 cm^{-1} were assigned to the N-H stretching vibrations of melamine (curve *ii*). The FT-IR spectrum of Py-M-COF (curve *iii*) revealed a C=N vibration band at

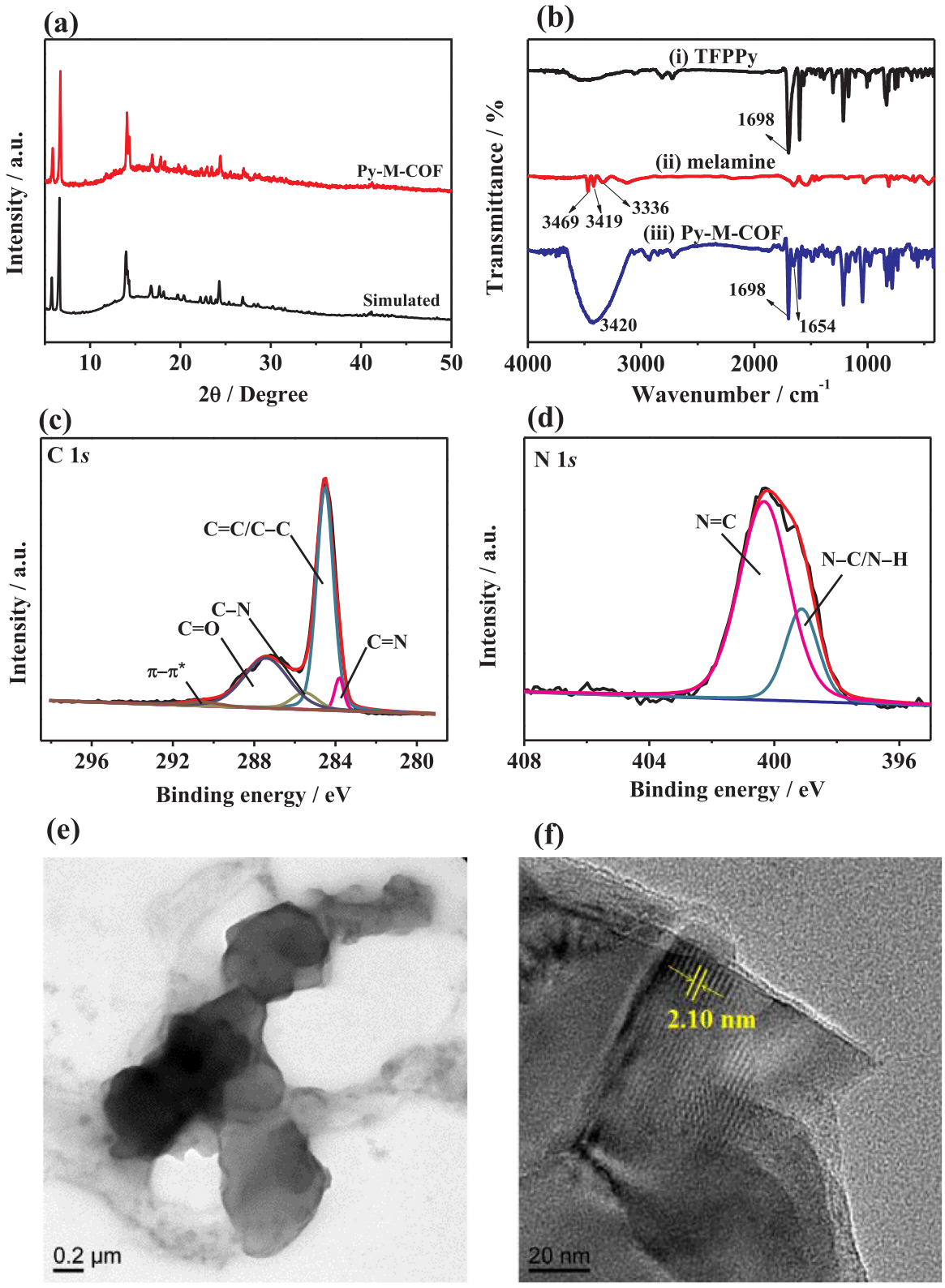

Fig. 1. Basic characterizations of Py-M-COF. (a) XRD pattern and (b) FT-IR spectrum; High-resolution (c) C 1 s and (d) N 1 s XPS spectra; (e, f) TEM images.

1654 cm^{-1} (Gao et al., 2018), indicating the successful condensation of TFPPy and melamine via the formation of imine bonds. Meanwhile, the characteristic peaks at 3420 and 1698 cm^{-1} were ascribed to the N-H stretching and C=O stretching vibrations, respectively. These functional groups are favorable to form hydrogen bond between the Py-M-COF and biomolecules (Li et al., 2017). Solid-state ^{13}C NMR spectroscopy of the Py-M-COF displayed characteristic resonance signals at δ = 166.4 (C=N), 190.1, 155.9, 145.4, 144.3, 132.4, 130.1, 126.8, 125.3, 123.1, and 122.4 ppm, further reflecting the presence of C=N vibration bonds (Fig. S2).

Additionally, XPS spectra were recorded to characterize the chemical structure and component of Py-M-COF. The XPS survey spectrum

showed three strong intensity peaks located at 284.6, 399.5, and 531.6 eV, which were due to C 1*s*, N 1*s*, and O 1*s*, respectively (Fig. S3**a**). Composition analysis of the sample revealed the following surface elemental composition: carbon (65.91%), nitrogen (16.79%), and oxygen (17.3%). The high-resolution C1*s* XPS spectrum of Py-M-COF could be deconvoluted into five component peaks (Fig. 1**c**), which were assigned to C=N at 283.8 eV, C=C/C-C at 284.6 eV, C-N at 285.5 eV, C=O at 287.4 eV, and π–π* at 290.6 eV (Lei et al., 2018). The high-resolution N1*s* XPS spectrum (Fig. 1**d**) could be fitted into two component peaks centered at 399.1 and 400.3 eV, which were assigned to N-C/N-H and N = C, respectively (Jin et al., 2012). The high-resolution O1*s* XPS spectrum of Py-M-COF (Fig. S3**b**) showed only one main component corresponding to O=C at 531.6 eV. Thereby, the XPS results further suggest the formation of C=N bonds and the successful synthesis of Py-M-COF. As known, the C=C, C=N, C=O, and NH_2 functional groups containing in Py-M-COF can facilitate in aptamer strands immobilization via π-π stacking interaction and electrostatic interaction (Gao et al., 2018).

Py-M-COF showed type IV N_2 adsorption-desorption isotherms with a hysteresis loop (Fig. S4**a**), which reflected a characteristic mesoporous structure. The Brunauer-Emmett-Teller surface area of COF was 495.5 $m^2 \cdot g^{-1}$, and the total pore volume was 0.62 $cm^3 \cdot g^{-1}$. The pore size distribution calculated by the Barrett–Joyner–Halenda method revealed a narrow distribution centered at 3.9 nm (Fig. S4**b**), further indicating the mesoporous structure of Py-M-COF.

3.3. Surface morphology of the as-prepared Py-M-COF nanostructure

The surface morphologies of the samples were characterized by scanning electron microscopy (SEM) and high-resolution transmission electron microscopy (HRTEM). As shown in Fig. S5**a** and **b**, the SEM images of the Py-M-COF revealed that it displayed a rough surface embedded with large, irregular particles. TEM images of the Py-M-COF illustrated that the large particles were composed of multilayer nanosheets with average size of around 0.6–1 μm (Fig. 1**e**). The HRTEM image of the Py-M-COF indicated that the pore channel is determined to be 2.10 nm (Fig. 1**f**). The large pore cavities and sheet-like structure in the Py-M-COF endowed the material with high charge carrier mobility (Wan et al., 2011), as well as rich anchoring sites for biomolecule immobilization (Peng et al., 2017).

Moreover, the basic characterizations of Py-g-C_3N_4 and Py-GO, including FT-IR, XRD, XPS, and SEM, are displayed in Figs. S6 and S7. The results confirmed the successful incorporation of g-C_3N_4 and GO-NH_2 in the Py-g-C_3N_4 and Py-GO hybrids, respectively.

3.4. Electrochemical sensing performances of Py-M-COF-based aptasensors toward ENR

3.4.1. Electrochemical performances of Py-M-COF-based aptasensors

EIS can effectively determine the changes in interfacial properties and processes associated with the conductive electrode surface. Fig. 2**a** shows the EIS Nyquist plots of the construction of the aptasensor and the detection procedure of ENR on the basis of the Py-M-COF-modified electrode. Bare AE displayed a small semicircle at high frequencies and a linear part at low frequencies (curve *i*), yielding a small R_{ct} of 0.10 kohm. When the bare AE was modified with the Py-M-COF layer, the R_{ct} value of Py-M-COF/AE slightly increased to 0.13 kohm (curve *ii*). The R_{ct} value of Py-M-COF/AE was smaller than those of previously reported modified materials, such as metal oxides (SnO_2 and TiO_2) (Zhang et al., 2016b, 2015), polymers (chitosan and polyaniline) (Liu et al., 2015a; Zhang et al., 2016a), carbon materials (graphene and multi-walled carbon nanotubes) (He et al., 2016; Wang et al., 2015a), and metal-organic frameworks (Zr-MOF and Al-MOF) (Guo et al., 2017; Liu et al., 2017a). This small value hinted the good electrochemical activity of the as-synthesized Py-M-COF and further boosted the sensitivity of the proposed electrochemical aptasensor. After the aptamer strands (Apt_{ENR}) were immobilized on the Py-M-COF-modified electrode surface, a large semicircle (R_{ct} = 0.34 kohm) was observed (curve *iii*) due to the electrostatic repulsion between negatively charged aptamers and negatively charged redox probe $[Fe(CN)_6]^{3-/4-}$, further hindering electron transfer (Hashkavayi et al., 2017). Moreover, the R_{ct} value further increased to 0.46 kohm with the incubation of target ENR molecules at 0.01 pg mL^{-1} (curve *iv*), which was due to the biomolecules blocking the charge transfer to the electrode surface. CV was also used to characterize the Py-M-COF-based aptasensor for detecting ENR in different steps. As shown in Fig. S8, the oxidation and reduction peak currents of $[Fe(CN)_6]^{3-/4-}$ at Py-M-COF/AE (curve *ii*) were smaller than those of bare AE (curve *i*), indicating that Py-M-COF reduced the electron transfer rate. As for Apt_{ENR}/Py-M-COF/AE (curve *iii*) and ENR/Apt_{ENR}/Py-M-COF/AE (curve *iv*), the currents decreased because the layers of aptamer strands and ENR molecules acted as barriers for electron transfer. The EIS and CV curves of aptasensors for detecting ENR on the basis of Py-g-C_3N_4- and Py-GO-modified electrodes are shown in Figs. S9 and S10, respectively. Similar trends were obtained.

Considering that the variation in R_{ct} ($\Delta R_{ct} = R_{ct,\ i+1} - R_{ct,\ i}$) represents the binding amount of the blocking layer (Sheikhzadeh et al., 2016), the ΔR_{ct} values calculated from each step during the detection process of ENR are summarized to compare the detection efficiency of different aptasensors, including the Py-M-COF-, Py-g-C_3N_4-, and Py-GO-based ones. As illustrated in Fig. 2**b**, three kinds of materials had high electrical conductivities with low ΔR_{ct} values. As compared with the Py-g-C_3N_4- and Py-GO-modified electrodes, the Py-M-COF-modified electrode had a higher ΔR_{ct} value both in aptamer immobilization and ENR detection step. Thus, the Py-M-COF-modified electrodes demonstrated high detection efficiency toward ENR. Py-M-COF with the extended π-conjugation framework could serve high charge carrier mobility and outstanding electrochemical conductivity for signal amplification (Wan et al., 2011). Moreover, the large specific surface area, microporous structure, and functional groups of the Py-M-COF nanosheets provided additional anchoring sites for aptamer immobilization through π-π stacking and electrostatic interactions, thereby improving its sensitivity. Therefore, the proposed Py-M-COF-based aptasensor may be an effective platform for ENR determination.

3.4.2. Optimization of conditions for detecting ENR

The operation conditions, such as concentration of aptamer and incubation time of target, can affect the electrochemical signals and sensitivity of analyte determination. As shown in Fig. 2**c**, the R_{ct} value during aptamer immobilization gradually increased with increasing ENR aptamer concentration, indicating that additional aptamer strands were anchored onto the surface of the Py-M-COF layer. The R_{ct} value was high when the concentration of ENR was 100 nM and then leveled off, indicating that the immobilization of aptamer strands onto Py-M-COF/AE was saturated. In addition, when the incubation time of ENR increased, the R_{ct} value at Apt_{ENR}/Py-M-COF/AE rose to a maximum response at 25 min and then slightly decreased to a steady value at 1 h (Fig. 2**d**). Therefore, the aptamer concentration of 100 nM and incubation time of ENR of 1 h were chosen as the optimal conditions for further measurements.

3.4.3. Sensitivity of Py-M-COF-based aptasensors toward ENR

To investigate the sensing performance of the Apt_{ENR}/Py-M-COF/AE assay in the quantitative analysis of ENR, we performed EIS measurements. As illustrated in Fig. 2**e**, the semicircle diameters increased as the ENR concentrations increased. Furthermore, the R_{ct} variation ($\Delta R_{ct} = R_{ct,ENR} - R_{ct,Apt}$) was proportional to the logarithmic of the ENR concentration within a wide range of 0.01–2000 pg mL^{-1} (Fig. 2**f**), where $R_{ct,ENR}$ and $R_{ct,Apt}$ are the R_{ct} values of Apt_{ENR}/Py-M-COF/AE before and after incubation with ENR, respectively. The corresponding linear regression equation is ΔR_{ct} (kohm) = 0.375 + 0.128 $\log C_{ENR}$ (pg mL^{-1}), with a correlation coefficient (R^2) of 0.994. The LOD was calculated as 6.07 fg mL^{-1} at a signal-to-noise ratio (S/N) of 3,

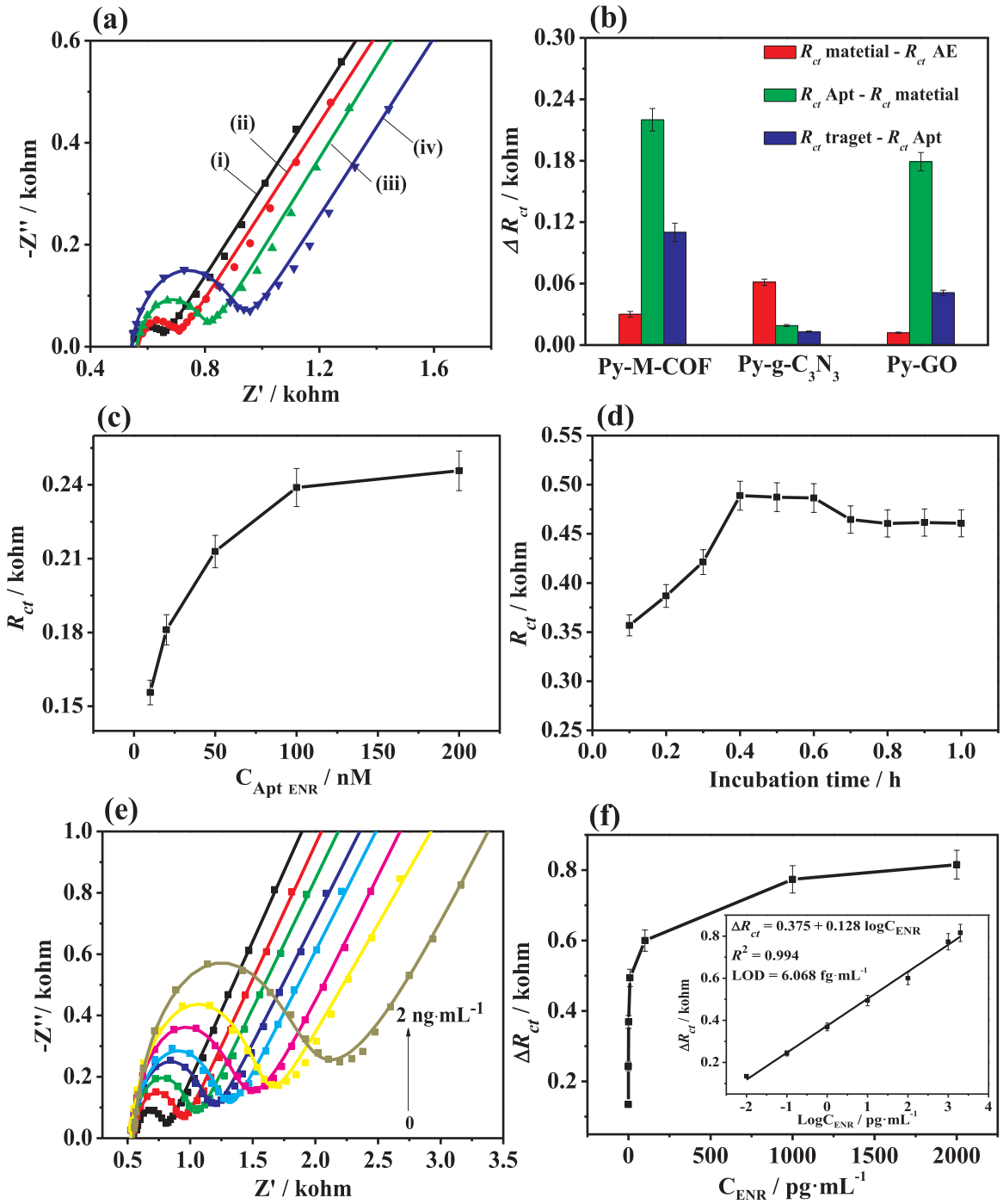

Fig. 2. (a) EIS Nyquist plots of the ENR detection procedure by the Py-M-COF-modified AE: (i) bare AE, (ii) Py-M-COF/AE, (iii) Apt_{ENR}/Py-M-COF/AE, (iv) ENR/Apt_{ENR}/Py-M-COF/AE in 0.01 M PBS (pH 7.4) containing 5.0 mM $[Fe(CN)_6]^{3-/4-}$. (b) The detection efficiency of the three kinds of aptasensors by using the variations of R_{ct} values before and after the ENR detection. Effects of (c) concentration of ENR aptamer and (d) incubation time of 0.01 pg mL^{-1} ENR on EIS response under different conditions. (e) EIS responses of the Apt_{ENR}/Py-M-COF/AE with different ENR concentrations (0, 0.01, 0.1, 1.0, 10.0, 100.0, 1000 and 2000 pg mL^{-1}). (f) Dependence of ΔR_{ct} on the concentration of ENR. Inset: calibration curves of ΔR_{ct} versus ENR concentration.

implying that the Py-M-COF-based aptasensor was highly sensitive toward ENR determination.

Additionally, the developed Apt_{AMP}/Py-M-COF/AE was applied to detect AMP (Fig. S11). A regression equation of ΔR_{ct} (kohm) = 0.701 + 0.186 $\log C_{AMP}$ (pg mL^{-1}) (R^2 = 0.997) was obtained within a linear range of 0.001–1000 pg mL^{-1}, yielding an ultralow LOD of 0.04 fg mL^{-1} (S/N = 3) toward AMP. These results demonstrated that the Py-M-COF could be an efficient biosensing platform for the ultrasensitive detection of antibiotics. Compared with the detection of ENR and AMP using other assays (Table 1 and Table S1), such as fluorescent, surface plasmon resonance, immunoassay, spectrophotometry, and electrochemical methods, the proposed Py-M-COF-based aptasensors presented the efficient determination of ENR and AMP with large detection ranges and LODs as low as the femtogram level. The high sensitivity of the proposed aptasensor was mainly attributed to the following features: (i) large specific surface area and porous frameworks can provide a large interface to the biomolecules (Lin et al., 2016), (ii) aptamer strands can attach on the COF matrix not only through π-π

Table 1
Comparison with other published work on ENR sensors.

Materials	Methods	Detection range	LOD	Refs.
11-mercapto-undecanoic acid (MUA)-modified electrode	EIS	1–1000 ng mL^{-1}	1.0 ng mL^{-1}	(Wu et al., 2009)
layer of oligo(phenylethynylene) molecular wire	Square wave voltammetry (SWV)	0.01–10 ng mL^{-1}	10 pg mL^{-1}	(Khor et al., 2011)
ENRO-ovalbumin conjugate	Surface plasmon resonance(SPR)	0.05–10 ng mL^{-1}	1.2 ng mL^{-1}	(Pan et al., 2017)
Immunoassay strip	Relative optical density (ROD)	0.3–24.3 ng mL^{-1}	0.935 ng mL^{-1}	(Zhao et al., 2008)
Apta-molecularly imprinted polymer/upconversion nanoparticles	Fluorescent	0.5–10 ng mL^{-1}	0.04 ng mL^{-1}	(Liu et al., 2017b)
Quantum dots (QDs)	Competitive fluorescence-linked immunosorbent assay (cFLISA)	1–100 ng mL^{-1}	2.5 ng mL^{-1}	(Chen et al., 2009)
Py-M-COF	EIS	0.01 pg mL^{-1}–2 ng mL^{-1}	6.07 fg mL^{-1}	**This work**

stacking and hydrogen-bonding interaction (Li et al., 2017) but also through the electrostatic interaction between terminal amino functional groups and negatively charged aptamers (Samanta and Sarkar, 2011), and (iii) the COF network facilitates charge transport and boosts sensitivity (Peng et al., 2017; Wan et al., 2011).

3.5. Selectivity, reproducibility, and stability of the proposed aptasensors

Concurrently, the other sensing performances, such as selectivity, reproducibility and storage stability, are also important for aptasensors. The selectivity of Apt_{ENR}/Py-M-COF/AE aptasensor or Apt_{AMP}/Py-M-COF/AE aptasensor to detect ENR or AMP (10 pg mL^{-1}) was tested with tetracycline, Kana, TOB, Na^+, K^+, streptomycin, and OTC at high concentrations of 100 pg mL^{-1}. As shown in Fig. 3**a** and Fig. S12**a**, negligible signal responses are obtained for the interference samples, suggesting the good selectivity of the developed aptasensors. In order to study the reproducibility of the aptasensor, five modified electrodes were prepared independently under the same conditions. The relative standard deviations (RSDs) of the ΔR_{ct} values are 1.25% for detecting 0.01 pg mL^{-1} of ENR and 1.44% for detecting 0.001 pg mL^{-1} of AMP (Fig. 3**b** and Fig. S12**b**), respectively. It demonstrates that as-fabricated electrochemical aptasensors exhibit good reproducibility. Furthermore, the storage stability of the aptasensors was assessed by measuring their electrochemical responses every day for 15 days while the aptasensor was stored at 4 °C when not in use. As shown in Fig. 3**c** and Fig. S12**c**, the ΔR_{ct} responses almost retain steady, implying the good stability. All these results indicate that the developed assays display good selectivity, high reproducibility, and excellent stability for detecting ENR and AMP.

3.6. Applicability of aptasensors

The ENR and AMP diluted in human serum samples were detected by the standard addition method to evaluate the feasibility of the proposed aptasensors. As shown in Table S2, the recoveries are 101.0–112.4% for ENR and 99.5–103.0% for AMP, respectively, which are well within the acceptable ranges. The RSD values are within the ranges of 1.52–4.58% for ENR and 2.51–3.51% for AMP, respectively. Therefore, the constructed Py-M-COF-based aptasensors also display good recoveries and have promising potential for the detection of antibiotics residues in biological fluids.

4. Conclusions

In summary, the Py-M-COF-based label-free electrochemical aptasensors were fabricated to detect trace antibiotics. Due to rich functional groups, large specific surface area and pore cavities of COF porous frameworks, larger amounts of aptamer strands were immobilized on the Py-M-COF in comparison with Py-g-C_3N_4 and Py-GO, resulting in high binding of target antibiotics. EIS measurements demonstrated that Py-M-COF-based aptasensors showed excellent electrochemical sensing performances and extremely low LODs of 6.07 and 0.04 fg·mL^{-1} for detecting ENR and AMP, respectively. Concurrently, other sensing features, including excellent selectivity, high reproducibility, good stability, and acceptable applicability in human serum samples, were observed for the electrochemical aptasensors. Because it is hard for the COF porous frameworks to be regularly nanosized, nevertheless, the formed electrode materials are usually uneven coated on the working electrode, further leading to the decline of the sensing performances in the practical applications.

Credit authorship Taxonomy statement

Minghua Wang: Validation, Formal analysis, Writing - original draft. **Mengyao Hu**: Methodology, Formal analysis, Investigation. **Jiameng Liu**: Methodology, Investigation. **Chuanpan Guo**: Visualization, Donglai Peng: Resources. **Qiaojuan Jia**: Formal analysis.

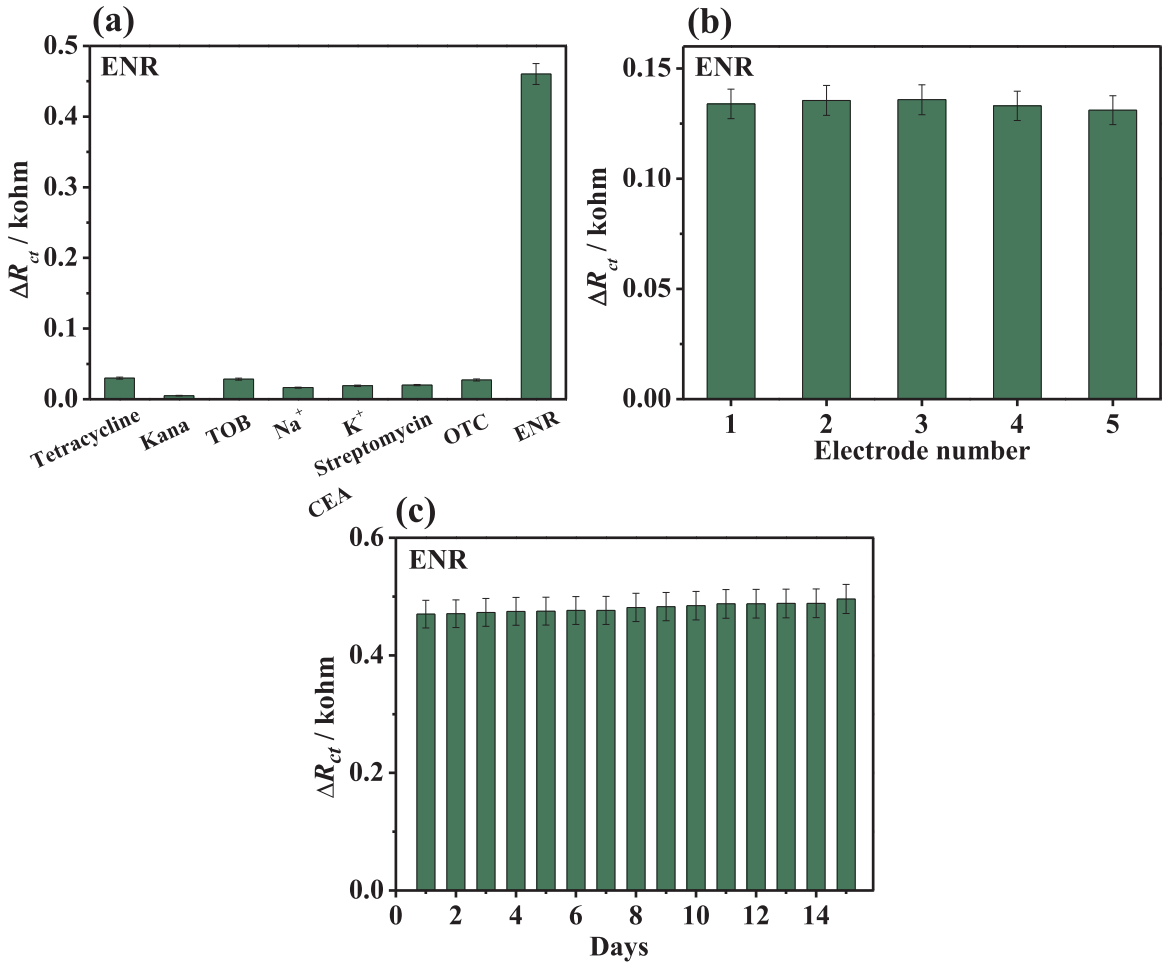

Fig. 3. (a) Selectivity, (b) reproducibility, and (c) stability assessment of the Py-M-COF-based aptasensor for detection of ENR.

Linghao He: Validation. **Zhihong Zhang**: Conceptualization, Writing - review & editing, Supervision. **Miao Du**: Formal analysis, Writing - review & editing

CRediT authorship contribution statement

Minghua Wang: Validation, Formal analysis, Writing - original draft. **Mengyao Hu:** Methodology, Formal analysis, Investigation. **Jiameng Liu:** Methodology, Investigation. **Chuanpan Guo:** Visualization. **Donglai Peng:** Resources. **Qiaojuan Jia:** Formal analysis. **Linghao He:** Validation. **Zhihong Zhang:** Conceptualization, Writing - review & editing, Supervision. **Miao Du:** Formal analysis, Writing - review & editing.

Acknowledgements

This work was supported by Programs for the National Natural Science Foundation of China (NSFC: Account Nos. U1604127 and 21601161), Innovative Technology Team of Henan Province (CXTD2014042), Scientific and Technological Project of Henan Province (192102310261, 192102310460), and Young Backbone Teacher Training Program in Universities of Henan Province (No. 2018GGJS089).

Declaration of interests

None.

Appendix A. Supporting information

Supplementary data associated with this article can be found in the online version at doi:10.1016/j.bios.2019.02.040.

References

Chen, J., Xu, F., Jiang, H., Hou, Y., Rao, Q., Guo, P., Ding, S., 2009. Food Chem. 113 (4), 1197–1201.
Chen, K., Abdolrhamani, M., Sheets, E., Freeman, J., Ward, G., White, J.L., 2017. J. Am. Chem. Soc. 139 (51), 18698–18704.
Chen, L., He, L., Ma, F., Liu, W., Wang, Y., Silver, M.A., Chen, L., Zhu, L., Gui, D., Diwu, J., Chai, Z., Wang, S., 2018. ACS Appl. Mater. Inter. 10 (18), 15364–15368.
Chen, X., Zhang, Q., Qian, C., Hao, N., Xu, L., Yao, C., 2015. Biosens. Bioelectron. 64 (22), 485–492.
Das, P., Mandal, S.K., 2018. J. Mater. Chem. A 6 (33), 16246–16256.
Ding, S.Y., Dong, M., Wang, Y.W., Chen, Y.T., Wang, H.Z., Su, C.Y., Wang, W., 2016. J. Am. Chem. Soc. 138 (9), 3031–3037.
Dolati, S., Ramezani, M., Nabavinia, M.S., Soheili, V., Abnous, K., Taghdisi, S.M., 2018. Anal. Biochem. 549, 124–129.
Du, P., Liu, S., Wu, P., Cai, C., 2007. Electrochim. Acta 53 (4), 1811–1823.
Gao, Q., Li, X., Ning, G.H., Leng, K., Tian, B., Liu, C., Tang, W., Xu, H.S., Loh, K.P., 2018. Chem. Commun. 54 (19), 2349–2352.
Guillerm, V., Gross, S., Serre, C., Devic, T., Bauer, M., Férey, G., 2010. Chem. Commun. 46 (5), 767–769.
Guo, C., Su, F., Song, Y., Hu, B., Wang, M., He, L., Peng, D., Zhang, Z., 2017. ACS Appl. Mater. Inter. 9 (47), 41188–41199.
Hashkavayi, A.B., Raoof, J.B., Ojani, R., Kavoosian, S., 2017. Biosens. Bioelectron. 92, 630–637.
He, L., Zhang, S., Wang, M., Peng, D., Yan, F., Zhang, Z., Zhou, L., 2016. Sens. Actuators B-Chem. 228, 500–508.
Huang, J.Y., Zhao, L., Lei, W., Wen, W., Wang, Y.J., Bao, T., Xiong, H.Y., Zhang, X.H., Wang, S.F., 2017. Biosens. Bioelectron. 99, 28–33.
Jin, K.H., In-Seob, B., Sang-Jin, C., Jin-Hyo, B., Byung-Cheo, L., Jinhee, H., Ilsub, C., Hong, B., 2012. Nanoscale Res. Lett. 7 (1), 30.

Khor, S.M., Liu, G., Peterson, J.R., Iyengar, S.G., Gooding, J.J., 2011. Electroanalysis 23 (8), 1797–1804.
Körbahti, B.K., Taşyürek, S., 2015. Environ. Sci. Pollut. R 22 (5), 3265–3278.
Lei, Z., Yang, Q., Xu, Y., Guo, S., Sun, W., Liu, H., Lv, L., Zhang, Y., Wang, Y., 2018. Nat. Commun. 9 (1), 576.
Li, F., Guo, Y., Wang, X., Sun, X., 2018. Biosens. Bioelectron. 115, 7–13.
Li, W., Yang, C., Yan, X., 2017. Chem. Commun. 53 (83), 11469–11471.
Li, Z., Zhang, Y., Xia, H., Mu, Y., Liu, X., 2016. Chem. Commun. 52 (39), 6613–6616.
Lin, G., Ding, H., Yuan, D., Wang, B., Wang, C., 2016. J. Am. Chem. Soc. 138 (10), 3302–3305.
Liu, C., Sun, C., Tian, J., Wang, Z., Ji, H., Song, Y., Zhang, S., Zhang, Z., He, L., Du, M., 2017a. Biosens. Bioelectron. 91, 804–810.
Liu, S., Kang, M., Yan, F., Peng, D., Yang, Y., He, L., Wang, M., Fang, S., Zhang, Z., 2015a. Electrochim. Acta 160, 64–73.
Liu, X., Qin, Y., Deng, C., Xiang, J., Li, Y., 2015b. Talanta 132, 150–154.
Liu, X., Ren, J., Su, L., Gao, X., Tang, Y., Ma, T., Zhu, L., Li, J., 2017b. Biosens. Bioelectron. 87, 203–208.
Luo, Z., Wang, Y., Lu, X., Chen, J., Wei, F., Huang, Z., Zhou, C., Duan, Y., 2017. Anal. Chim. Acta 984, 177–184.
Medina, D.D., Sick, T., Bein, T., 2017. Adv. Energy Mater. 7 (16), 1700387.
Pan, M., Li, S., Wang, J., Sheng, W., Wang, S., 2017. Sensors 17 (9), 1984.
Peng, Y., Huang, Y., Zhu, Y., Chen, B., Wang, L., Lai, Z., Zhang, Z., Zhao, M., Tan, C., Yang, N., Shao, F., Han, Y., Zhang, H., 2017. J. Am. Chem. Soc. 139 (25), 8698–8704.
Qin, X., Yin, Y., Yu, H., Guo, W., Pei, M., 2016. Biosens. Bioelectron. 77, 752–758.
Samanta, D., Sarkar, A., 2011. Chem. Soc. Rev. 40 (5), 2567–2592.
Sheikhzadeh, E., Chamsaz, M., Turner, A.P.F., Jager, E.W.H., Beni, V., 2016. Biosens. Bioelectron. 80, 194–200.
Singh, H., Tomer, V.K., Jena, N., Bala, I., Sharma, N., Nepak, D., Sarkar, A.D., Kailasam, K., Pal, S.K., 2017. J. Mater. Chem. A 5, 21820–21827.
Soler, M.A.G., 2018. J. Magn. Magn. Mater. 467, 37–48.
Song, K.M., Jeong, E., Jeon, W., Cho, M., Ban, C., 2012. Anal. Bioanal. Chem. 402 (6), 2153.
Sun, J., Klechikov, A., Moise, C., Prodana, M., Enachescu, M., Talyzin, A.V., 2017. Angew. Chem. Int. Ed. 57 (4), 1034–1038.
Syska, J., 2013. Phys. Rev. E 88 (3), 32130.
Tang, Y., Li, M., Gao, X., Liu, X., Gao, J., Ma, T., Li, J., 2017. Microchim. Acta 184 (9), 3469–3475.
Wan, S., Gándara, F., Asano, A., Furukawa, H., Saeki, A., Dey, S.K., Liao, L., Ambrogio, M.W., Botros, Y.Y., Duan, X., Seki, S., Stoddart, J.F., Yaghi, O.M., 2011. Chem. Mater. 23 (18), 4094–4097.
Wang, J., Ma, K., Yin, H., Zhou, Y., Ai, S., 2017. Microchim. Acta 185 (1), 68.
Wang, M., Kang, M., Guo, C., Fang, S., He, L., Jia, C., Zhang, G., Bai, B., Zong, W., Zhang, Z., 2015a. Electrochim. Acta 182, 668–675.
Wang, M., Zhang, S., Ye, Z., Peng, D., He, L., Yan, F., Yang, Y., Zhang, H., Zhang, Z., 2015b. Microchim. Acta 182 (13), 2251–2258.
Wu, C., Lin, C., Wang, W., 2009. Talanta 79 (1), 62–67.
Xiang, Z., Cao, D., 2012. Macromol. Rapid Commun. 33 (14), 1184–1190.
Xu, W., Yi, H., Yuan, Y., Pei, J., Chai, Y., Yuan, R., Wilson, G.S., 2015. Biosens. Bioelectron. 64, 423–428.
Yang, Y., Yang, Z., Lv, J., Yuan, R., Chai, Y., 2017a. Talanta 169, 44–49.
Yang, Z., Ding, X., Guo, Q., Wang, Y., Lu, Z., Ou, H., Luo, Z., Lou, X., 2017b. Sens. Actuators B-Chem. 253, 1129–1136.
Yu, F., Yu, S., Yu, L., Li, Y., Wu, Y., Zhang, H., Qu, L., Harrington, P.D.B., 2014. Food Chem. 149, 71–75.
Yu, Z., Sutlief, A.L., Lai, R.Y., 2018. Sens. Actuators B-Chem. 258, 722–729.
Zhai, R., Gong, X., Xie, J., Yuan, Y., Xu, F., Jiang, Y., Huang, Z., Dai, X., Zhang, Y., Qian, X., Fang, X., 2019. Talanta 191, 553–560.
Zhang, W., Duan, D., Liu, S., Zhang, Y., Leng, L., Li, X., Chen, N., Zhang, Y., 2018. Biosens. Bioelectron. 118, 129–136.
Zhang, W., Qiu, L.G., Yuan, Y.P., Xie, A.J., Shen, Y.H., Zhu, J.F., 2012. J. Hazard. Mater. 221–222 (4), 147–154.
Zhang, W., Zhang, Z., Li, Y., Chen, J., Li, X., Zhang, Y., Zhang, Y., 2017. Sens. Actuators B-Chem. 247, 756–764.
Zhang, X., Xie, X., Wang, H., Zhang, J., Pan, B., Xie, Y., 2013. J. Am. Chem. Soc. 135 (1), 18–21.
Zhang, Z., Duan, F., He, L., Peng, D., Yan, F., Wang, M., Zong, W., Jia, C., 2016a. Microchim. Acta 183 (3), 1089–1097.
Zhang, Z., Ji, H., Zhang, S., Peng, D., Fu, Q., Wang, M., He, L., Yue, L., 2016b. New J. Chem. 40 (1), 755–763.
Zhang, Z., Zhai, S., Wang, M., He, L., Peng, D., Liu, S., Yang, Y., Fang, S., Zhang, H., 2015. Anal. Methods-UK 7 (11), 4725–4733.
Zhao, Y., Zhang, G., Liu, Q., Teng, M., Yang, J., Wang, J., 2008. J. Agr. Food Chem. 56 (24), 12138–12142.